Sandwich Nanoarchitecture of Si/Reduced Graphene Oxide Bilayer Nanomembranes for Li-Ion Batteries with Long Cycle Life

Xianghong Liu,*,[†] Jun Zhang,[⊥] Wenping Si,[†,‡] Lixia Xi,[∥] Barbara Eichler,[†] Chenglin Yan,*,[†,§] and Oliver G. Schmidt[†,‡]

[†]Institute for Integrative Nanosciences, IFW-Dresden, Helmholtzstrasse 20, 01069 Dresden, Germany, [‡]Material Systems for Nanoelectronics, Chemnitz University of Technology, Reichenhainerstrasse 70, 09107 Chemnitz, Germany, [§]College of Physics, Optoelectronics and Energy & Collaborative Innovation Center of Suzhou Nano Science and Technology, Soochow University, 215006 Suzhou, China, [⊥]Institut für Chemie, Humboldt-Universität zu Berlin, Brook-Taylor-Strasse 2, 12489 Berlin, Germany, and [∥]Institute for Complex Materials, IFW-Dresden, Helmholtzstrasse 20, 01069 Dresden, Germany

ABSTRACT The large capacity loss and huge volume change of silicon anodes severely restricts their practical applications in lithium ion batteries. In this contribution, the sandwich nanoarchitecture of rolled-up Si/reduced graphene oxide bilayer nanomembranes was designed *via* a strain released strategy. Within this nanoarchitecture, the inner void space and the mechanical feature of nanomembranes can help to buffer the strain during lithiation/delithiation; the alternately stacked conductive rGO layers can protect the Si layers from excessive formation of SEI layers. As anodes for lithium-ion batteries, the sandwiched Si/rGO nanoarchitecture demonstrates long cycling life of 2000 cycles at 3 A g^{-1} with a capacity degradation of only 3.3% per 100 cycles.
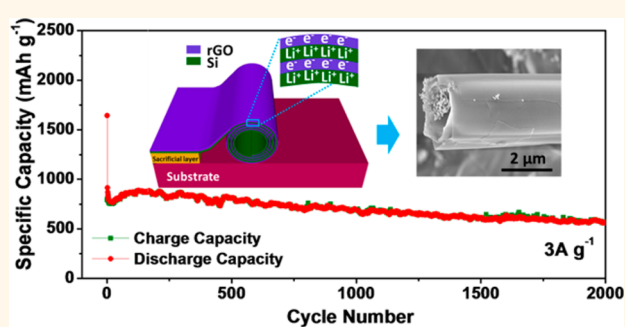
KEYWORDS: silicon · reduced graphene oxide · nanomembranes · nanoarchitecture · lithium-ion batteries

Silicon is regarded as one of the most promising anode materials for the next generation lithium-ion batteries (LIBs) benefiting from its highest theoretical capacity (~4200 mAh g^{-1}), environmental benignity, abundance in nature, and low working potential.[1,2] However, the dramatic volume change (>300%) during lithiation to Li$_x$Si ($0 \leq x \leq 4.4$) often leads to the rapid cracking and pulverization of the material structure;[3] the excessive formation of solid electrolyte interphase (SEI) layer consumes too much lithium ions and electrolyte thus causes a large capacity loss.[2] Therefore, the cycling performance of silicon anodes is still far from satisfactory from a viewpoint of practical applications. These critical problems are proposed to be alleviated by designing appropriate nanostructures and encapsulation with protective coatings.[4−6] Nanostructures can accelerate Li$^+$ diffusion kinetics, provide large electrode/electrolyte interfacial contact area, and relax the strain

of lithiation/delithiation with available surrounding free space.[7,8] Various Si nanostructures such as nanoparticles,[9] nanowires,[6,10] the double-walled SiO$_x$/Si nanotubes,[2] and nanosheets,[11] mesoporous silicon sponge,[12] demonstrated greatly improved performance. Meanwhile, flexible conductive protecting coatings are also widely used to improve the cycling performance with the attempt to accommodate the volume change and prevent the aggregation of nanoparticles.[1] For example, improved electrochemical properties have been reported on the pomegranate-structured Si/SiO$_2$/Carbon,[13] Si@void@C yolk−shell structures,[14] silicon nanowires coated with carbon and conducting polymer,[15,16] graphene encapsulated Si nanoparticles,[17,18] carbon nanotubes−Si films,[19] and core−shell structure with Si nanoparticles embedded in carbon fibers.[20]

With two-dimensional (2D) geometry and lateral dimension at least 2 orders of
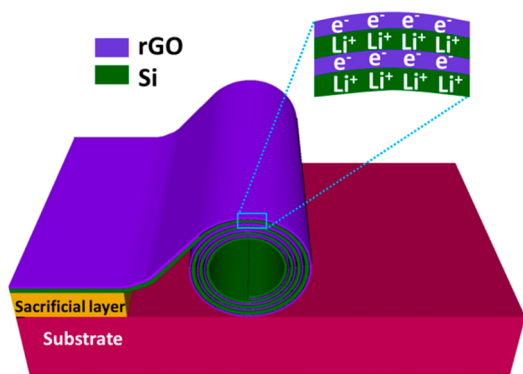
Figure 1. Schematic fabrication process of the rolled-up Si/rGO bilayer nanomembranes.

magnitude larger than the thickness,[21,22] nanomembranes can not only combine the merits of the 0D and 1D counterparts but also be the ideal candidate for 3D structures.[23] The 2D geometry endows the nanomembranes with mechanical feature to be deformable into various mechanical-engineered wavy, helical and rolled-up 3D architectures.[22,24,25] This mechanical feature is particularly expected to buffer the strain of lithiation/delithiation,[26−28] and delay the pulverization of the electrode materials for LIBs. On the other hand, graphene and reduced graphene oxide (rGO) are an ideal protective material for the electrode materials and have shown great potential in improving battery performance.[18,29−33] With good flexibility, graphene and rGO are highly compatible with the strain engineering strategy. In this contribution, the sandwich nanoarchitecture of Si/rGO bilayer nanomembranes is designed by combining the merits of nanomembranes and rGO protecting layer, which demonstrates good capacity retention and long cycling life as anode materials for LIBs.

RESULTS AND DISCUSSION

The Si/rGO bilayer nanomembrane consists of the parallel aligned Si and rGO nanolayers with the Si nanolayer as the electrochemically active layer for lithium storage and the rGO nanolayer as conductive protecting layer. The sandwich nanoarchitecture of Si/rGO bilayer nanomembranes is fabricated *via* strain released strategy with the assistance of a sacrificial layer. As illustrated in Figure 1, the Si/rGO bilayer nanomembranes are forced to roll up naturally under the built-in strain released by selectively etching away the sacrificial layer. And the sandwich structure is formed by the rolled up nanomembrane with multilayer convoluting. The alternately stacked elastic rGO layers can protect the Si layers from being directly exposed to electrolyte and prevent the aggregation of Si layers. The void space inside this configuration can well accommodate the volume change of Si layers and relax the strain during lithiation/delithiation. All these structural advantages are conflated within the

sandwich-nanostructured bilayer nanomembranes, which are expected to potentially improve the electrochemical performance for LIBs.

The scanning electron microscopy (SEM) image (Figure 2a) exhibits the morphology of the as-obtained rolled-up Si/rGO bilayer nanomembranes with the length of several hundreds of micrometers. The inset of Figure 2a displays the multilayer convoluted nanoarchitecture at one end of a single rolled-up nanomembrane. The cross section images of a single rolled-up nanomembrane after focused ion beam (FIB) cutting clearly reveal the large inner void space (Figure 2b) and the multilayer stacking (Supporting Information Figure S1). The TEM image (Figure 2c) of a single rolled-up nanomembrane also reveals the multilayer convoluted tubular structure with different diameters. Herein, the packing density of the rolled-up nanomembrane is defined as the fraction of the cylinder space filled by single rolled-up nanomembrane. For the rolled-up Si/rGO bilayer nanomembrane shown in Figure 2b, the packing density is calculated to be ∼16.03%. The material density of the Si/rGO bilayer nanomembrane is calculated to be ∼2.28 g cm^{-3}. The related calculation can be seen in the Supporting Information. The bulk density of the rolled-up Si/rGO bilayer nanomembranes is ∼2.91 mg cm^{-3}. The composition is analyzed to be Si, C, and O by energy-dispersive X-ray spectroscopy (EDX), as shown in the element mapping images (Figure 2e−g) of Figure 2d. The thickness of a single dispersed rGO sheet is determined to be ∼2.0 nm by atomic force microscopy (AFM) (see Supporting Information Figure S3), corresponding to the thickness of two elementary rGO sheets (The thickness of an elementary GO or rGO sheet is about 1.0−1.4 nm.[34]). Figure 2h shows the AFM line scan image of the spin-coated rGO nanolayer with the thickness of ∼15.8 nm. The composition and structure of the rolled-up Si/rGO bilayer nanomembranes were further characterized by Raman spectroscopy. As shown in Figure 2i, the Raman peak at ∼470 cm^{-1} is ascribed to the vibration mode of the typical transverse optical structure (TO) in amorphous Si,[35] while the two peaks at ∼1363 and ∼1595 cm^{-1} are attributed to the disordered band (D band) and the graphitic band (G band) of the graphitic carbon sheets in rGO.[36]

The electrochemical properties of the sandwich nanoarchitectured Si/rGO bilayer nanomembranes as anodes for LIBs were evaluated by cyclic voltammetry (CV), electrochemical impedance spectroscopy (EIS) and galvanostatic discharge/charge cycling with Swagelok-type half-cells. Figure 3a shows the initial three CV curves of the Si/rGO bilayer nanomembrane electrode. In the first discharge process, the minor peak at 0.98 V is related to the formation of SEI layer, and the main cathodic peak from 0.49 nearly to ∼0 V, evolving into two peaks at 0.15 and ∼0 V in the subsequent cycles, arises from the alloying process of amorphous
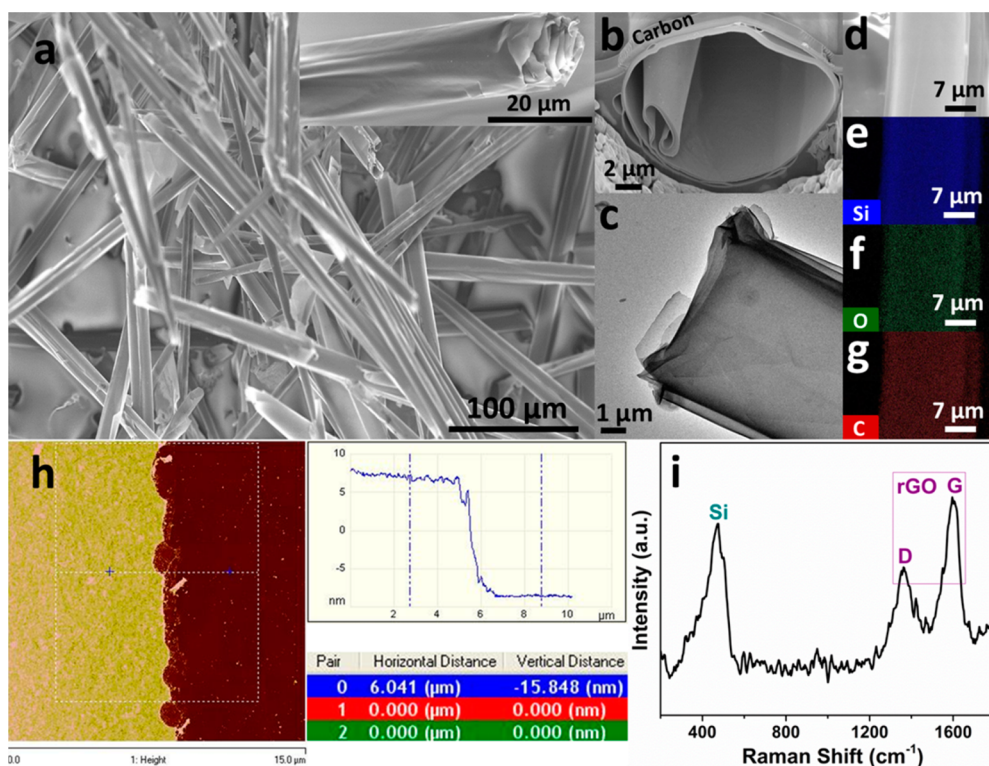
Figure 2. Characterizations of the rolled-up Si/rGO bilayer nanomembranes: (a) SEM image (inset: a single rolled-up nanomembrane); (b) cross section image of a single rolled-up nanomembrane after FIB cutting (carbon is the leftover after FIB cutting); (c) TEM image of a single rolled-up nanomembrane; (e) Si, (f) O, and (g) C elemental mapping images of (d) from EDX; (h) AFM image of the spin-coated rGO layer with corresponding line scan and thickness, and (i) Raman spectrum.

silicon with Li to form a series of Li$_x$Si alloys ($0 \leq x \leq 4.4$).[6] The anodic peak at 0.52 V in the first cycle, which appears as two peaks at 0.52 and 0.4 V in the subsequent cycles, corresponds to the dealloying process of Li$_x$Si to amorphous Si.[37,38] Figure 3b exhibits the representative galvanostatic discharge/charge voltage curves at the current density of 1 A g^{-1} within 0.01−1.5 V. The long slopes (below 0.5 V) are related to the reversible lithiation/delithiation of silicon, which is in accordance with the CV peaks.

The electrochemical impedance spectroscopy (EIS) was used to further study the charge transfer and ion diffusion kinetics of the Si nanomembrane and Si/rGO bilayer nanomembrane electrodes. Both Nyquist plots in Figure 3c exhibit an incomplete semicircle in the high frequency region and a straight line in the low frequency region. Compared with the pure Si electrode, the Si/rGO electrode shows a reduced diameter of the semicircle, indicating the decreased charge transfer (ct) resistance at the electrode/solution interface due to the conductive rGO layer.[39] In the frequency range between 10−1 Hz, the slope of the linear fitting plot of Z′ versus $\omega^{-1/2}$ defines the Warburg factor (Figure 3d), which reflects the solid-state diffusion of Li$^+$ inside the electrode materials.[40] The lower slope of the fitting line indicates the reduced solid-state diffusion inside the Si/rGO electrode.

The cycling performance of the Si/rGO bilayer nanomembrane electrode is first evaluated at 100 mA g^{-1}, and the comparison with that of the Si nanomembrane electrode is shown in Figure 4a. The Si nanomembrane electrode has an initial discharge/charge capacity of 2683/1250 mAh g^{-1} with the initial Coulombic efficiency (CE) of 46.6%. The reversible capacity in the second cycle is 1237 mAh g^{-1} (CE: 95.5%), and the reversible capacity after 100 cycles is 1231 mAh g^{-1} (CE: 99.0%), which demonstrates the structural advantages of nanomembranes in the cycling performance. The Si/rGO bilayer nanomembrane electrode delivers a higher initial discharge/charge capacity of 2871/1817 mAh g^{-1} with a higher initial CE of 63.3% than the Si nanomembrane electrode. The reversible capacity in the second cycle is 1732 mAh g^{-1} (CE: 94.0%), and then the capacity decreases slightly in the initial several cycles. Afterward the electrode keeps a stable cycling with the reversible capacity of about 1500 ± 50 mAh g^{-1} (CE: $98.2 \pm 0.4\%$). The reversible capacity after 100 cycles is 1433 mAh g^{-1} (CE: 97.6%). The higher initial CE and higher reversible capacity of the Si/rGO electrode than the Si electrode confirms the important role of the rGO protecting layers in the capacity retention. Supporting Information Figure S4 shows another cycling performance comparison at 100 mA g^{-1}, indicating the good repeatability.
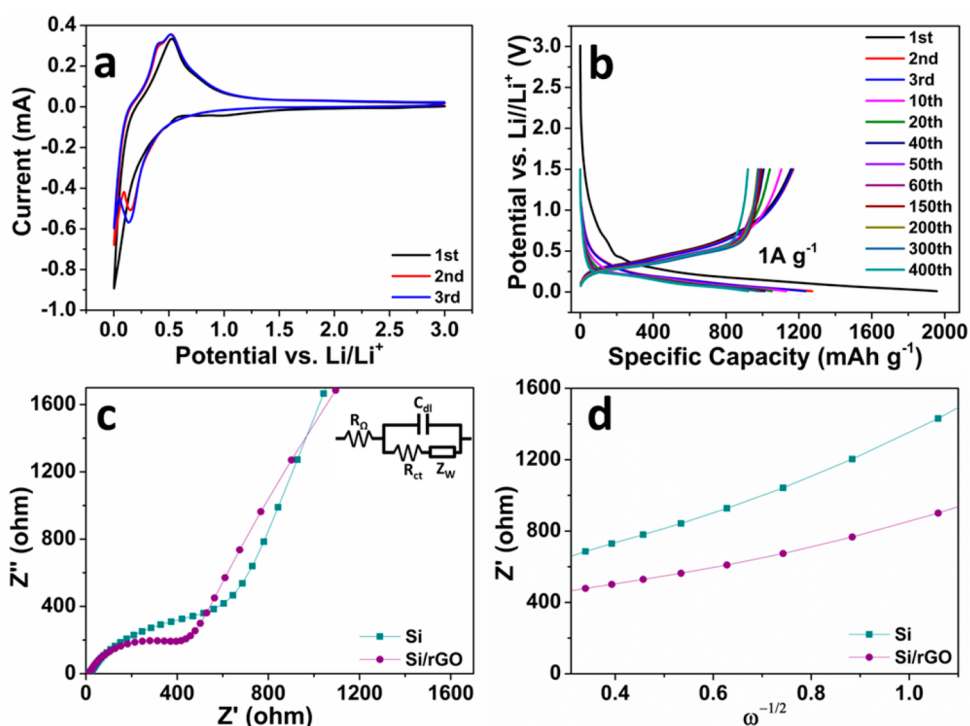
Figure 3. Electrochemical properties of the Si/rGO bilayer nanomembrane electrodes: (a) CV curves at a scan rate of 0.1 mV s^{-1} within 0.003−3.0 V vs Li/Li$^+$; (b) representative discharge/charge voltage curves at 1 A g^{-1} within 0.01−1.5 V vs Li/Li$^+$ (except for the first discharge curve starting from 3.0 V); (c) Nyquist plots and (d) the relationship between Z′ and $\omega^{-1/2}$ within 10−1 Hz of the Si and Si/rGO electrode obtained from EIS (symbols, real data; lines, fitting curves) within 100 kHz to 1 mHz (perturbation voltage: 10 mV) at the fixed voltage of 3.0 V before cycling. Inset of (c) is the simplified electrochemical system as Randles circuit, in which R_Ω is ohmic resistance, C_{dl} is double-layer capacitance, R_{ct} is charge transfer resistance, and Z_W is Warburg impedance.

The cycling performance of the Si/rGO bilayer nanomembrane electrode is further examined at a higher current density of 1 A g^{-1}, as shown in Figure 4b. The electrode offers an initial discharge/charge capacity of 1957/1155 mAh g^{-1} (CE: 59.0%). After the capacity decay in the initial several cycles, the electrode keeps a stable cycling with the reversible capacity of about 965 ± 50 mAh g^{-1} during the 25th−530th cycles. The reversible capacity after 700 cycles is 821 mAh g^{-1} (CE: ~99.8%). The cycling performance of the Si nanomembrane electrode at 1 A g^{-1} is shown in Supporting Information Figure S5. The initial discharge/charge capacity is 1737/667 mAh g^{-1} (CE: 38.4%) and the reversible capacity after 350 cycles is 806 mAh g^{-1}. The reversible capacity of the Si/rGO bilayer nanomembrane electrode after 350 cycles is 957 mAh g^{-1}, also demonstrating the improved performance of Si/rGO electrodes. Figure 4c shows the cycling performance at an even higher current density of 3 A g^{-1} for 2000 cycles. The initial discharge/charge capacity is 1642/792 mAh g^{-1} and the reversible capacity fluctuates within ~815 ± 65 mAh g^{-1} for the 16−600 cycles. The capacity only degrades by 3.3% per 100 cycles for the total 2000 cycles. Even after 2000 cycles, the electrode still delivers a much higher reversible capacity of 571 mAh g^{-1} than the theoretical capacity (372 mAh g^{-1}) of graphite.

The rate capability of the Si/rGO bilayer nanomembrane electrode is evaluated by three turns of rate cycling measurements with a stepwise current density program from 0.3 to 15 A g^{-1}, as shown in Figure 4d. During the initial 0.3 A g^{-1} step, the first discharge/charge capacity is 2545/1249 mAh g^{-1} and the reversible capacity after 40 cycles is 1248 mAh g^{-1}. Then the capacity decreases gradually with increasing the current density. Although the capacity decreases slightly at each current density in the first turn due to the further formation of SEI layer at higher current rate, the electrode keeps a stable cycling at each current density in the subsequent two turns of measurement. When the current density is set back to 0.3 A g^{-1} after each turn of measurement, the capacity can recover to a similar value of the last cycle in the initial 0.3 A g^{-1} step and keeps a very stable cycling. The reversible capacity of the last cycle at 0.3, 0.7, 1.5, 3, 7, and 15 A g^{-1} in the third turn is 1263 (the 165th cycle), 1146, 952, 636, 325, 111 mAh g^{-1}, respectively. Even after a long heavy-duty operation for three turns of rate cycling, the electrode still keeps a very stable long cycling at 0.3 A g^{-1} with a reversible capacity of 1245 mAh g^{-1} after 250 cycles (last 0.3 A g^{-1} step), demonstrating the good reversibility of the Si/rGO bilayer nanomembrane electrode. The rate capability of the Si nanomembrane electrode with the same measurement program can be
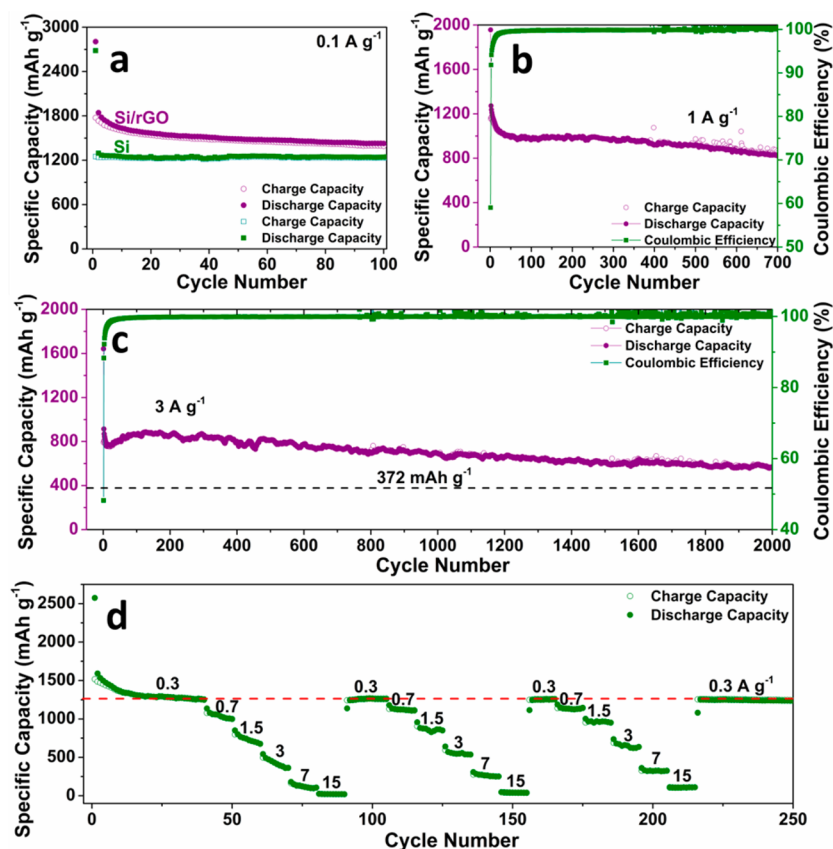
Figure 4. Cycling performance at (a) 100 mA g^{-1} (in comparison with the Si nanomembrane electrode), (b) 1 A g^{-1}, and (c) 3 A g^{-1}; (d) rate capability of the Si/rGO bilayer nanomembrane electrodes within 0.01−1.5 V *vs* Li/Li$^+$. The specific capacity is calculated based on the total weight of Si and rGO.

seen in Supporting Information Figure S6. At the initial 0.3 A g^{-1} step, the first discharge/charge capacity is 2146/950 mAh g^{-1} and the reversible capacity after 40 cycles is 1010 mAh g^{-1}. The reversible capacity of the last cycle at 0.3, 0.7, 1.5, 3, 7, and 15 A g^{-1} in the third turn is only 1082 (the 165th cycle), 979, 778, 544, 259, 1.48 mAh g^{-1}, respectively. By comparison, it can be seen that the Si/rGO bilayer nanomembrane electrode exhibits better rate capability with improved capacity retention than the Si nanomembrane electrode.

The electrochemical performance of the Si/rGO bilayer nanomembrane electrode is compared with the reference results (see Supporting Information Table S1). From comparison, it can be seen that the present Si/rGO bilayer nanomembrane electrode does not register the best performance among all the Si-based anodes. For example, the double-walled SiO$_x$/Si nanotubes,[2] pomegranated Si/SiO$_2$/Carbon,[13] Si@void@C yolk−shell structures,[14] Si/Ni/PVDF coaxial nanofiber,[41] delivered longer cycling life or higher capacity compared with the Si/rGO bilayer nano-membrane electrode. Compared with these nanostructures, the rolled-up nanomembranes have a large size of about 5−20 μm in diameter and hundreds of microns in length with lower surface-to-volume ratio correspondingly. In addition, only one surface of the Si

nanomembranes is protected by rGO layers with the other surface still being exposed to the electrolyte. However, the electrochemical performance of the Si/rGO bilayer nanomembrane electrode still outperforms quite a large part of the Si-based anodes.

The lithium storage capability of the Si/rGO bilayer nanomembrane electrode benefits preferably from the structural advantages of the multilayer convoluted sandwich nanoarchitecture. The amorphous structure can facilitate the lithiation process and accommodate the strain in the first cycle.[42−44] The mechanical feature makes the nanomembranes deformable to buffer the strain during lithiation/delithiation, thus maintaining the structural integrity against pulverization. This is confirmed by the morphology change of the Si/rGO bilayer nanomembrane before and after cycling. Before cycling, the rolled-up nanomembranes have well-defined tubular profile (Supporting Information Figure S7a), and the large inner void space can be seen from the cross section image of a single rolled-up nanomembrane after FIB cutting (Supporting Information Figure S7b). After repeated expansion/shrinking during rate capability measurement for 250 cycles, the tubular structures are not obvious from the top view of the electrode (Supporting Information Figure S7c). However, from the cross section image after FIB cutting
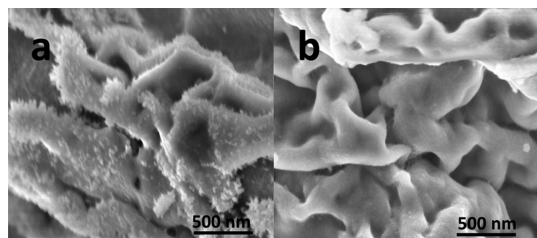
Figure 5. SEI layer on the surface of the Si/rGO bilayer nanomembrane after rate capability measurement for 250 cycles: (a) without and (b) with rGO layer.

(Supporting Information Figure S7d), it can be seen that the rolled-up structure deforms greatly with reduced inner void space due to the inward expansion to buffer the strain; the nanomembranes become considerably wrinkled under the strain during cycling but still maintain high structural integrity. The wrinkled nanomembranes after cycling can also be seen from the TEM images in Supporting Information Figure S8. Meanwhile, as a conductive buffering network, the alternately stacked elastic rGO protecting layers can facilitate the electron transport, accommodate the volume change of Si layers and prevent their aggregation. Some additional lithium storage may be also provided between rGO sheets. Furthermore, the rGO layers can protect Si layers from being directly exposed to the electrolyte, which can help to suppress the excessive formation of SEI layer and slow down the capacity decay. The protection role of the rGO layers is clearly revealed by the SEM observation of the wrinkled Si/rGO bilayer nanomembranes after rate capability measurement for 250 cycles. It can be seen that the surface of the Si layer without the protection of rGO layer becomes quite rougher due to the pronounced formation of SEI layer (Figure 5a) than the other surface with rGO protecting layer (Figure 5b).

CONCLUSION

The sandwich nanoarchitecture of rolled-up Si/rGO bilayer nanomembranes are designed *via* strain released strategy, and exhibit long cycling lifetime of 2000 cycles at 3 A g^{-1} with a capacity degradation of only 3.3% per 100 cycles as anode for LIBs. The inner void space inside the configuration together with the mechanical feature of the amorphous Si nanomembranes can buffer the strain of lithiation/delithiation against pulverization to extend cycling life. The alternatively aligned rGO layers in this nanostructure can facilitate electron transport, accommodate the volume change of Si layers and prevent their aggregation. Furthermore, the rGO layers can protect the nanomembranes from the excessive formation of thick SEI layer to suppress the capacity degradation.

METHODS

Synthesis of rGO. First, graphite oxide was synthesized by modified Hummers' method from natural graphite, and then sonicated into graphene oxide (GO) colloid.[45,46] The rGO was obtained by reducing GO with NaBH$_4$ at 95 °C for 3 h, after which the resulting mixture was filtered and washed thoroughly by deionized water until the pH of filtrate to be 7.0. The obtained rGO was then redispersed in water and sonicated into suspension with the concentration of ~4.0 mg mL^{-1} for subsequent use.

Fabrication of the Sandwich Nanoarchitecture of Si/rGO Bilayer Nanomembranes. As for the fabrication of the Si/rGO bilayer nanomembranes, photoresist AR-P 3510 as a sacrificial layer was first spin-coated onto a Si wafer substrate, and a 25 nm silicon film was sequentially deposited onto the sacrificial layer by an electron beam evaporator (Edwards AUTO50) with bulk Si source (Kurt J. Lesker) at the pressure of ~6 × 10^{-6} mbar. The thickness of the deposited film is controlled by a quartz crystal microbalance, and the tooling factor was calibrated beforehand by depositing a 200 nm film the actual thickness of which was then measured by a Profilometer Dektak XT (Bruker). Then the rGO suspension was spin-coated onto the deposited silicon nanofilm and dried naturally at room temperature. The spin-coating process was repeated several times to obtain the desired thickness. By selectively etching away the underlying photoresist with acetone, the Si/rGO bilayer nanomembranes are forced to roll up naturally to form the multilayer convoluted sandwich nanoarchitecture, as schemed in Figure 1. The obtained rolled-up nanomembranes were thoroughly washed with acetone for several times and then dried in a critical point dryer (CPD). For comparison, the pure Si rolled-up nanomembranes with the same thickness were fabricated by the same process without rGO spin-coating.

Material Characterization. The overall morphology of the rolled-up Si/rGO bilayer nanomembranes was observed by scanning electron microscopy (SEM, DSM 982, Zeiss). The composition was characterized by scanning electron microscopy (SEM, LEO, GEMINI, 1530) and energy-dispersive X-ray spectroscopy (EDX, Bruker XFlash Detector 4010). Raman spectroscopy (Renishaw) was performed at a 442 nm wavelength to identify the composition. The thickness of individual rGO sheet was determined by atomic force microscopy (AFM, Dimension 3100 equipped with controller Nanoscope V). To determine the thickness of the spin-coated rGO layer on Si nanolayer, the rGO was spin-coated on the O$_2$ plasma treated Si wafer (with the same spin-coating condition as the sample fabrication), patterned by photolithography, and finally measured by AFM. Transmission electron microscopy (TEM) was performed on Philips CM200 LaB$_6$. The cross section of the rolled-up nanomembranes was observed by the SEM (NVision 40 CrossBeam, Carl Zeiss) after focused ion beam (FIB) etching.

Electrochemical Measurements. Electrochemical measurements were performed with two-electrode Swagelok-type half-cells assembled in Ar-filled glovebox (H$_2$O, O$_2$ < 0.1 ppm, Mbraun, Germany). To make the working electrode, the rolled-up Si/rGO bilayer nanomembranes were vibrating mixed with conductive additive carbon black (Timcal) and sodium alginate (Aldrich) binder (7:2:1 by weight) in water using a vibromixer (Analog Vortex Mixer, VWR). Then the obtained paste was coated onto a Cu foil (Goodfellow) current collector and finally dried at 60 °C for 10 h in vacuum oven. The dried electrode plate, with the active electrode material areal density of ~0.53 mg cm^{-2} (total weight of Si and rGO), was punched into several discs with ϕ = 10 mm (the electrode area is 0.785 cm^2) for batteries assembly. The battery was assembled with a punched electrode disc as working electrode, a Li foil (ϕ = 10 mm) as counter/reference electrode and a glass fiber membrane (Whatman) as separator, as well as the electrolyte which contains the solution of 1 mol L^{-1} LiPF$_6$ in ethylene carbonate/dimethyl carbonate/diethyl carbonate (1:1:1, wt %, Merck) including 2 wt % vinylene

carbonate (Merck) electrolyte additive. Galvanostatic discharge/charge cycling was performed with a multichannel battery-testing system (Arbin BT 2000) within 0.01−1.5 V vs Li/Li$^+$ at different current densities. Cyclic voltammetry (CV) at the scan rate of 0.1 mV s^{-1} within 0.003−3.0 V vs Li/Li$^+$ and electrochemical impedance spectroscopy (EIS) within 100 kHz to 1 mHz with a perturbation voltage of 10 mV at fixed voltage of 3.0 V before cycling were performed on Zahner electrochemical workstation (IM6) with an assembled half-cell at room temperature.

Supporting Information Available: Cross section image of the multilayer stack, calculation of the packing density and material density, AFM image of a single rGO sheet, the repeatability of cycling performance at 100 mA g^{-1} of the Si and Si/rGO bilayer nanomembrane electrodes, cycling performance at 1 A g^{-1} and rate capability of the Si nanomembrane electrodes, SEM and TEM images of the Si/rGO bilayer nanomembrane before and after cycling, electrochemical performance comparison of various Si-based anodes summarized in table. This material is available free of charge *via* the Internet at http://pubs.acs.org.

REFERENCES AND NOTES

1. Su, X.; Wu, Q.; Li, J.; Xiao, X.; Lott, A.; Lu, W.; Sheldon, B. W.; Wu, J. Silicon-Based Nanomaterials for Lithium-Ion Batteries: A Review. *Adv. Energy Mater*, DOI: 10.1002/aenm.201300882.

2. Wu, H.; Chan, G.; Choi, J. W.; Ryu, I.; Yao, Y.; McDowell, M. T.; Lee, S. W.; Jackson, A.; Yang, Y.; Hu, L.; et al. Stable Cycling of Double-Walled Silicon Nanotube Battery Anodes through Solid-Electrolyte Interphase Control. *Nat. Nanotechnol.* **2012**, *7*, 310−315.

3. Beaulieu, L. Y.; Eberman, K. W.; Turner, R. L.; Krause, L. J.; Dahn, J. R. Colossal Reversible Volume Changes in Lithium Alloys. *Electrochem. Solid-State Lett.* **2001**, *4*, A137−A140.

4. Kasavajjula, U.; Wang, C. S.; Appleby, A. J. Nano- and Bulk-Silicon-Based Insertion Anodes for Lithium-Ion Secondary Cells. *J. Power Sources* **2007**, *163*, 1003−1039.

5. Magasinski, A.; Dixon, P.; Hertzberg, B.; Kvit, A.; Ayala, J.; Yushin, G. High-Performance Lithium-Ion Anodes Using a Hierarchical Bottom-up Approach. *Nat. Mater.* **2010**, *9*, 353−358.

6. Chan, C. K.; Peng, H. L.; Liu, G.; McIlwrath, K.; Zhang, X. F.; Huggins, R. A.; Cui, Y. High-Performance Lithium Battery Anodes Using Silicon Nanowires. *Nat. Nanotechnol.* **2008**, *3*, 31−35.

7. Arico, A. S.; Bruce, P.; Scrosati, B.; Tarascon, J. M.; Van Schalkwijk, W. Nanostructured Materials for Advanced Energy Conversion and Storage Devices. *Nat. Mater.* **2005**, *4*, 366−377.

8. Bruce, P. G.; Scrosati, B.; Tarascon, J.-M. Nanomaterials for Rechargeable Lithium Batteries. *Angew. Chem., Int. Ed.* **2008**, *47*, 2930−2946.

9. Favors, Z.; Wang, W.; Bay, H. H.; Mutlu, Z.; Ahmed, K.; Liu, C.; Ozkan, M.; Ozkan, C. S. Scalable Synthesis of Nano-Silicon from Beach Sand for Long Cycle Life Li-Ion Batteries. *Sci. Rep.* **2014**, *4*, 5623.

10. Liu, B.; Wang, X.; Chen, H.; Wang, Z.; Chen, D.; Cheng, Y.-B.; Zhou, C.; Shen, G. Hierarchical Silicon Nanowires-Carbon Textiles Matrix as a Binder-Fee Anode for High-Performance Advanced Lithium-Ion Batteries. *Sci. Rep.* **2013**, *3*, 1622.

11. Lu, Z. Y.; Zhu, J. X.; Sim, D. H.; Zhou, W. W.; Ship, W. H.; Hng, H. H.; Yan, Q. Y. Synthesis of Ultrathin Silicon Nanosheets by Using Graphene Oxide as Template. *Chem. Mater.* **2011**, *23*, 5293−5295.

12. Li, X.; Gu, M.; Hu, S.; Kennard, R.; Yan, P.; Chen, X.; Wang, C.; Sailor, M. J.; Zhang, J.-G.; Liu, J. Mesoporous Silicon Sponge as an Anti-Pulverization Structure for High-Performance Lithium-Ion Battery Anodes. *Nat. Commun.* **2014**, *5*, 4105.

13. Liu, N.; Lu, Z.; Zhao, J.; McDowell, M. T.; Lee, H.-W.; Zhao, W.; Cui, Y. A Pomegranate-Inspired Nanoscale Design for Large-Volume-Change Lithium Battery Anodes. *Nat. Nanotechnol.* **2014**, *9*, 187−192.

14. Liu, N.; Wu, H.; McDowell, M. T.; Yao, Y.; Wang, C.; Cui, Y. A Yolk-Shell Design for Stabilized and Scalable Li-Ion Battery Alloy Anodes. *Nano Lett.* **2012**, *12*, 3315−3321.

15. Bogart, T. D.; Oka, D.; Lu, X.; Gu, M.; Wang, C.; Korgel, B. A. Lithium Ion Battery Peformance of Silicon Nanowires with Carbon Skin. *ACS Nano* **2013**, *8*, 915−922.

16. Yao, Y.; Liu, N.; McDowell, M. T.; Pasta, M.; Cui, Y. Improving the Cycling Stability of Silicon Nanowire Anodes with Conducting Polymer Coatings. *Energy Environ. Sci.* **2012**, *5*, 7927−7930.

17. Wen, Y.; Zhu, Y. J.; Langrock, A.; Manivannan, A.; Ehrman, S. H.; Wang, C. S. Graphene-Bonded and -Encapsulated Si Nanoparticles for Lithium Ion Battery Anodes. *Small* **2013**, *9*, 2810−2816.

18. Zhou, X.; Yin, Y.-X.; Wan, L.-J.; Guo, Y.-G. Self-Assembled Nanocomposite of Silicon Nanoparticles Encapsulated in Graphene through Electrostatic Attraction for Lithium-Ion Batteries. *Adv. Energy Mater.* **2012**, *2*, 1086−1090.

19. Cui, L. F.; Hu, L. B.; Choi, J. W.; Cui, Y. Light-Weight Free-Standing Carbon Nanotube-Silicon Films for Anodes of Lithium Ion Batteries. *ACS Nano* **2010**, *4*, 3671−3678.

20. Hwang, T. H.; Lee, Y. M.; Kong, B.-S.; Seo, J.-S.; Choi, J. W. Electrospun Core−Shell Fibers for Robust Silicon Nano-particle-Based Lithium Ion Battery Anodes. *Nano Lett.* **2011**, *12*, 802−807.

21. Huang, G. S.; Mei, Y. F. Thinning and Shaping Solid Films into Functional and Integrative Nanomembranes. *Adv. Mater.* **2012**, *24*, 2517−2546.

22. Rogers, J. A.; Lagally, M. G.; Nuzzo, R. G. Synthesis, Assembly and Applications of Semiconductor Nanomembranes. *Nature* **2011**, *477*, 45−53.

23. Nikoobakht, B.; Li, X. L. Two-Dimensional Nanomem-branes: Can They Outperform Lower Dimensional Nanocrystals? *ACS Nano* **2012**, *6*, 1883−1887.

24. Schmidt, O. G.; Eberl, K. Nanotechnology: Thin Solid Films Roll up into Nanotubes. *Nature* **2001**, *410*, 168−168.

25. Kim, D. H.; Rogers, J. A. Bend, Buckle, and Fold: Mechanical Engineering with Nanomembranes. *ACS Nano* **2009**, *3*, 498−501.

26. Deng, J.; Ji, H.; Yan, C.; Zhang, J.; Si, W.; Baunack, S.; Oswald, S.; Mei, Y.; Schmidt, O. G. Naturally Rolled-up C/Si/C Trilayer Nanomembranes as Stable Anodes for Lithium-Ion Batteries with Remarkable Cycling Performance. *Angew. Chem., Int. Ed.* **2013**, *52*, 2326−2330.

27. Zhang, L.; Deng, J.; Liu, L.; Si, W.; Oswald, S.; Xi, L.; Kundu, M.; Ma, G.; Gemming, T.; Baunack, S.; et al. Hierarchically Designed SiO$_x$/SiO$_y$ Bilayer Nanomembranes as Stable Anodes for Lithium Ion Batteries. *Adv. Mater.* **2014**, *26*, 4527−4532.

28. Yu, C.; Li, X.; Ma, T.; Rong, J.; Zhang, R.; Shaffer, J.; An, Y.; Liu, Q.; Wei, B.; Jiang, H. Silicon Thin Films as Anodes for High-Performance Lithium-Ion Batteries with Effective Stress Relaxation. *Adv. Energy Mater.* **2012**, *2*, 68−73.

29. Luo, J.; Zhao, X.; Wu, J.; Jang, H. D.; Kung, H. H.; Huang, J. Crumpled Graphene-Encapsulated Si Nanoparticles for Lithium Ion Battery Anodes. *J. Phys. Chem. Lett.* **2012**, *3*, 1824−1829.

30. Kucinskis, G.; Bajars, G.; Kleperis, J. Graphene in Lithium Ion Battery Cathode Materials: A Review. *J. Power Sources* **2013**, *240*, 66−79.

31. Zhou, G.; Wang, D.-W.; Li, F.; Zhang, L.; Li, N.; Wu, Z.-S.; Wen, L.; Lu, G. Q.; Cheng, H.-M. Graphene-Wrapped Fe$_3$O$_4$ Anode Material with Improved Reversible Capacity and

Cyclic Stability for Lithium Ion Batteries. *Chem. Mater.* **2010**, *22*, 5306–5313.

32. Tao, H.-C.; Fan, L.-Z.; Mei, Y.; Qu, X. Self-Supporting Si/Reduced Graphene Oxide Nanocomposite Films as Anode for Lithium Ion Batteries. *Electrochem. Commun.* **2011**, *13*, 1332–1335.

33. Guo, S.; Dong, S. Graphene Nanosheet: Synthesis, Molecular Engineering, Thin Film, Hybrids, and Energy and Analytical Applications. *Chem. Soc. Rev.* **2011**, *40*, 2644–2672.

34. Eda, G.; Chhowalla, M. Chemically Derived Graphene Oxide: Towards Large-Area Thin-Film Electronics and Optoelectronics. *Adv. Mater.* **2010**, *22*, 2392–2415.

35. Brodsky, M. H.; Cardona, M.; Cuomo, J. J. Infrared and Raman Spectra of the Silicon-Hydrogen Bonds in Amorphous Silicon Prepared by Glow Discharge and Sputtering. *Phys. Rev. B* **1977**, *16*, 3556–3571.

36. Ferrari, A. C.; Meyer, J. C.; Scardaci, V.; Casiraghi, C.; Lazzeri, M.; Mauri, F.; Piscanec, S.; Jiang, D.; Novoselov, K. S.; Roth, S.; et al. Raman Spectrum of Graphene and Graphene Layers. *Phys. Rev. Lett.* **2006**, *97*, 187401.

37. Baranchugov, V.; Markevich, E.; Pollak, E.; Salitra, G.; Aurbach, D. Amorphous Silicon Thin Films as a High Capacity Anodes for Li-Ion Batteries in Ionic Liquid Electrolytes. *Electrochem. Commun.* **2007**, *9*, 796–800.

38. Huggins, R. A. Lithium Alloy Negative Electrodes. *J. Power Sources* **1999**, *81*, 13–19.

39. Wang, L.; Ye, Y. J.; Lu, X. P.; Wen, Z. B.; Li, Z.; Hou, H. Q.; Song, Y. H. Hierarchical Nanocomposites of Polyaniline Nanowire Arrays on Reduced Graphene Oxide Sheets for Supercapacitors. *Sci. Rep.* **2013**, *3*, 3568.

40. Gao, H. Y.; Jiao, L. F.; Peng, W. X.; Liu, G.; Yang, J. Q.; Zhao, Q. Q.; Qi, Z.; Si, Y. C.; Wang, Y. J.; Yuan, H. T. Enhanced Electrochemical Performance of $LiFePO_4$/C *via* Mo-Doping at Fe Site. *Electrochim. Acta* **2011**, *56*, 9961–9967.

41. Xiao, Q.; Zhang, Q.; Fan, Y.; Wang, X.; Susantyoko, R. A. Soft Silicon Anodes for Lithium Ion Batteries. *Energy Environ. Sci.* **2014**, *7*, 2261–2268.

42. Jiang, Y.; Zhang, D.; Li, Y.; Yuan, T.; Bahlawane, N.; Liang, C.; Sun, W.; Lu, Y.; Yan, M. Amorphous Fe_2O_3 as a High-Capacity, High-Rate and Long-Life Anode Material for Lithium Ion Batteries. *Nano Energy* **2014**, *4*, 23–30.

43. Li, X. F.; Meng, X. B.; Liu, J.; Geng, D. S.; Zhang, Y.; Banis, M. N.; Li, Y. L.; Yang, J. L.; Li, R. Y.; Sun, X. L.; et al. Tin Oxide with Controlled Morphology and Crystallinity by Atomic Layer Deposition onto Graphene Nanosheets for Enhanced Lithium Storage. *Adv. Funct. Mater.* **2012**, *22*, 1647–1654.

44. Wang, X.-L.; Han, W.-Q.; Chen, H.; Bai, J.; Tyson, T. A.; Yu, X.-Q.; Wang, X.-J.; Yang, X.-Q. Amorphous Hierarchical Porous GeO_x as High-Capacity Anodes for Li Ion Batteries with Very Long Cycling Life. *J. Am. Chem. Soc.* **2011**, *133*, 20692–20695.

45. Hummers, W. S.; Offeman, R. E. Preparation of Graphitic Oxide. *J. Am. Chem. Soc.* **1958**, *80*, 1339–1339.

46. Marcano, D. C.; Kosynkin, D. V.; Berlin, J. M.; Sinitskii, A.; Sun, Z.; Slesarev, A.; Alemany, L. B.; Lu, W.; Tour, J. M. Improved Synthesis of Graphene Oxide. *ACS Nano* **2010**, *4*, 4806–4814.